

# Supplementary information

## Solution-processed hybrid graphene flake/2H-MoS<sub>2</sub> quantum dot heterostructures for electrochemical hydrogen evolution

Leyla Najafi<sup>†,‡,‡</sup>, Sebastiano Bellani<sup>†,‡</sup>, Beatriz Martín-García<sup>†,§</sup>, Reinier Oropesa-Nuñez<sup>†</sup>, Antonio Esau Del Rio Castillo<sup>†</sup>, M. Prato<sup>⊥</sup>, I. Moreels<sup>†,§</sup>, and F. Bonaccorso<sup>\*,†</sup>

<sup>†</sup> *Graphene Labs, Istituto Italiano di Tecnologia, via Morego 30, 16163 Genova, Italy.*

<sup>‡</sup> *Università degli studi di Genova, Dipartimento di Chimica e Chimica Industriale, Via Dodecaneso 31, 16163 Genova, Italy.*

<sup>§</sup> *Nanochemistry Departiment, Istituto Italiano di Tecnologia, via Morego 30, 16163 Genova, Italy.*

<sup>⊥</sup> *Materials Characterization Facility, Istituto Italiano di Tecnologia, via Morego 30, 16163 Genova, Italy.*

<sup>‡</sup> These authors contributed equally.

\* Corresponding author: [francesco.bonaccorso@iit.it](mailto:francesco.bonaccorso@iit.it)

## S.1 Experimental Methods

### S.1.1 Synthesis

2H-MoS<sub>2</sub> quantum dots (QDs) are produced through a one-step solvothermal method starting from 2H-MoS<sub>2</sub> flakes, produced by liquid phase exfoliation (LPE)<sup>1,2,3</sup> of bulk MoS<sub>2</sub> crystals in 2-Propanol (IPA) followed by sedimentation-based separation (SBS).<sup>1,4,5</sup> In detail, 30 mg of MoS<sub>2</sub> bulk crystal (Sigma Aldrich) are added to 50 mL of IPA and then ultrasonicated (Branson® 5800 cleaner, Branson Ultrasonics) for 8 h. The resulting dispersion is ultracentrifuged (Optima™ XE-90 ultracentrifuge, Beckman Coulter) for 15 min at 2700 *g*, in order to separate the un-exfoliated and thick MoS<sub>2</sub> crystals (collected as sediment) from the thinner 2H-MoS<sub>2</sub> flakes that remain in the supernatant. An aliquot (*i.e.* 10 mL) of the as-obtained 2H-MoS<sub>2</sub> flakes dispersion is kept for further characterization (sample I), while the rest is refluxed in air under stirring for 24 h at 140 °C. The resulting dispersion is subsequently ultracentrifuged for 30 min at 24600 *g*. Afterward, the supernatant is collected, thus obtaining the 2H-MoS<sub>2</sub> QDs dispersion (sample II).

The 1T-MoS<sub>2</sub> flakes are produced by a chemical lithium intercalation method.<sup>1,6</sup> Briefly, 500 mg of MoS<sub>2</sub> bulk crystals are suspended in 10 mL of 1.6 M methyllithium (CH<sub>3</sub>Li) in diethylether (Sigma Aldrich) and 10 mL of 1.6 M *n*-butyllithium (*n*-BuLi) in cyclohexane (Sigma Aldrich). The dispersion is stirred for 3 days at room temperature under argon atmosphere. The Li-intercalated material (Li<sub>*x*</sub>MoS<sub>2</sub>) is separated by vacuum filtration under Ar atmosphere.<sup>7</sup> Li<sub>*x*</sub>MoS<sub>2</sub> is washed in anhydrous hexane to remove non-intercalated Li ions and organic residues. Li<sub>*x*</sub>MoS<sub>2</sub> powder is then exfoliated by ultrasonication in deionized (DI) water for 1 h. The dispersion is ultrasonicated for 10 min and then ultracentrifuged for 40 min at 67000 *g*. The collected precipitate is rinsed with MilliQ water and re-dispersed in 400 mL of IPA. The resulting dispersion is ultrasonicated for 30 min and ultracentrifuged for 20 min at 17000 *g*. The supernatant is then collected, thus obtaining the 1T-MoS<sub>2</sub> flake dispersion.

The graphene flake dispersion is produced by LPE of graphite in *N*-Methyl-2-pyrrolidone (NMP).<sup>1,5</sup> 1 g of graphite is dispersed in 100 mL of NMP and ultrasonicated for 6 hours. The obtained dispersion is ultracentrifuged at 17000 *g* for 50 min at 15 °C. Finally, 80% of the supernatant is collected by pipetting, thus obtaining graphene flake dispersion.

### S.1.2 Material characterization

Transmission electron microscopy (TEM) images are taken with a JEM 1011 (JEOL) transmission electron microscope, operating at 100 kV. Samples for the TEM measurements are prepared by drop-casting the 2H-MoS<sub>2</sub> flakes, 2H-MoS<sub>2</sub> QDs, 1T-MoS<sub>2</sub> flakes and graphene flake dispersions onto carbon-coated copper grids. Their lateral dimensions are measured using ImageJ software (NIH). Statistical TEM analysis is carried out by means of Origin 8.1 software (OriginLab).

Atomic force microscopy (AFM) images are taken using a Nanowizard III (JPK Instruments, Germany) mounted on an Axio Observer D1 (Carl Zeiss, Germany) inverted optical microscope. The AFM measurements are carried out by using PPP-NCHR cantilevers (Nanosensors, USA) with a nominal tip diameter of 10 nm. A drive frequency of ~295 kHz is used. Intermittent contact mode AFM images of 2.5×2.5 μm<sup>2</sup> and 500×500 nm<sup>2</sup> are collected with 512 data points per line and the working set point is kept above 70% of the free

oscillation amplitude. The scan rate for acquisition of images is 0.7 Hz. Height profiles are processed by using the JPK Data Processing software (JPK Instruments, Germany) and the data are analyzed with OriginPro 9.1 software. Statistical AFM analysis is carried out by means of Origin 8.1 software (OriginLab) on four different AFM images for each sample. The samples are prepared by drop-casting 2H-MoS<sub>2</sub> flakes, 2H-MoS<sub>2</sub> QDs, 1T-MoS<sub>2</sub> flakes and graphene flake dispersions onto mica sheets (G250-1, Agar Scientific Ltd., Essex, U.K.).

X-ray photoelectron spectroscopy (XPS) is carried out on a Kratos Axis UltraDLD spectrometer, using a monochromatic Al K<sub>α</sub> source (15 kV, 20 mA). The spectra are taken on a 300 μm x 700 μm area. Wide scans are collected with constant pass energy of 160 eV and energy step of 1 eV; high-resolution spectra are acquired at constant pass energy of 10 eV and energy step of 0.1 eV. The binding energy scale is internally referenced to the C 1s peak at 284.8 eV. The spectra are analyzed using the CasaXPS software (version 2.3.17). The fitting of the spectra is performed by using a linear background and Voigt profiles. The samples are prepared by drop-casting dispersions of 2H-MoS<sub>2</sub> flakes, 2H-MoS<sub>2</sub> QDs, 1T-MoS<sub>2</sub> flakes and graphene flakes onto Si/SiO<sub>2</sub> substrate (LDB Technologies Ltd). The graphene flakes sample is also annealed at 350 C° in order to remove residual NMP.

The crystal structure is characterized by X-ray diffraction (XRD) using a PANalytical Empyrean with CuKα radiation. The samples for XRD are prepared by drop-casting 2H-MoS<sub>2</sub> flakes, 2H-MoS<sub>2</sub> QDs, and 1T-MoS<sub>2</sub> flakes dispersions on a silicon wafer and dried under vacuum.

The optical absorption spectroscopy (OAS) measurements are carried out using a Cary Varian 6000i UVvis-NIR spectrometer using quartz cuvette with a path length of 1 cm. The 2H-MoS<sub>2</sub> flakes, 2H-MoS<sub>2</sub> QDs and 1T-MoS<sub>2</sub> flakes are characterized as-produced, while for the graphene flakes, a 1:10 dilution of the corresponding dispersion is measured in order to avoid scattering losses. The corresponding solvent baselines are subtracted.

The steady-state photoluminescence (PL) emission measurements are performed using an Edinburgh Instruments FLS920 spectrofluorometer. The PL spectra are collected exciting the samples at different wavelengths ranging from 280 to 500 nm at a step of 20 nm, using a Xe lamp coupled to a monochromator. The 2H-MoS<sub>2</sub> QDs dispersions are contained in a quartz glass cuvette with a path length of 1 cm. To discard any contribution from the solvent (isopropanol), blank (control) measurement is carried out in the same experimental conditions used for the characterization of the aforementioned samples.

Raman measurements are carried out by using a Renishaw microRaman invia 1000 using a 50× objective, with an excitation wavelength of 532 nm and an incident power on the samples of 1 mW. For each sample, 50 spectra are collected. The samples are prepared by drop casting dispersions of 2H-MoS<sub>2</sub> flakes, 2H-MoS<sub>2</sub> QDs, and 1T-MoS<sub>2</sub> flakes and graphene flakes onto Si/SiO<sub>2</sub> (300 nm SiO<sub>2</sub>) substrates and dried under vacuum. The spectra are fitted with Lorentzian functions. Statistical analysis is carried out by means of Origin 8.1 software (OriginLab).

### ***S.1.3 Fabrication of the electrodes***

Dispersions of 2H-MoS<sub>2</sub> flakes, 2H-MoS<sub>2</sub> QDs, and 1T-MoS<sub>2</sub> flakes are deposited on glassy carbon (GC) sheets (Sigma Aldrich) (GC/2H-MoS<sub>2</sub> flakes, GC/2H-MoS<sub>2</sub> QDs and GC/1T-MoS<sub>2</sub> flakes, respectively) by drop-casting (mass loading of 0.5 mg/cm<sup>2</sup>). Flexible hybrid heterostructures of graphene flakes (graphene), graphene flakes/2H-MoS<sub>2</sub> flakes

(graphene/2H-MoS<sub>2</sub> flakes) and graphene flakes/2H-MoS<sub>2</sub> QDs (graphene/2H-MoS<sub>2</sub> QDs) or 1T-MoS<sub>2</sub> flakes (graphene/1T-MoS<sub>2</sub> flakes) are fabricated by sequentially depositing graphene flakes and MoS<sub>2</sub> flakes or QDs dispersions onto nylon membranes with size pore of 0.2 μm (Whatman® membrane filters nylon, Sigma Aldrich) through a vacuum filtration process (MoS<sub>2</sub> mass loading of 0.5 mg/cm<sup>2</sup>). All the electrodes are dried overnight at room temperature before their electrochemical characterization.

#### **S.1.4 Electrodes characterization**

The AFM images of the flexible electrodes (*i.e.*, graphene, graphene/2H-MoS<sub>2</sub> flakes and the graphene/2H MoS<sub>2</sub> QDs) are taken using the same set-up used for AFM characterization of materials.

Electrochemical measurements on the as-prepared electrodes are carried out at room temperature in a flat-bottom fused silica cell under a three-electrode configuration using CompactStat potentiostat/galvanostat station (Ivium), controlled via Ivium's own IviumSoft. A Pt wire is used as the counter-electrode and saturated KCl Ag/AgCl is used as the reference electrode. Measurements are carried out in 200 mL 0.5 M H<sub>2</sub>SO<sub>4</sub> (99.999% purity, Sigma Aldrich) (pH 1). Oxygen is purged from electrolyte by flowing N<sub>2</sub> gas throughout the liquid volume using a porous frit for 30 minutes before starting the measurements. A constant N<sub>2</sub> flow is maintained afterwards for the whole duration of the experiments, to avoid re-dissolution of molecular oxygen in the electrolyte. Potential difference between the working electrode and the Ag/AgCl reference electrode is converted to the reversible hydrogen electrode (RHE) scale via the Nernst equation:  $E_{RHE} = E_{Ag/AgCl} + 0.059pH + E_{Ag/AgCl}^0$ , where  $E_{RHE}$  is the converted potential versus RHE,  $E_{Ag/AgCl}$  is the experimental potential measured against the Ag/AgCl reference electrode, and  $E_{Ag/AgCl}^0$  is the standard potential of Ag/AgCl at 25 °C (0.1976 V). Polarization curves are acquired at a 5 mV/s scan rate. Polarization curves from all catalysts are *iR*-corrected, where *i* is the current and the *R* is the series resistance arising from the substrate and electrolyte resistances. *R* is measured by electrochemical impedance spectroscopy (EIS) at open circuit potential and at frequency of 10<sup>4</sup> Hz.

The linear portions of the Tafel plots are fit to the Tafel equation  $\eta = b \cdot \log(j) + A$ ,<sup>8,9</sup> where  $\eta$  is the overpotential with respect to the reversible hydrogen electrode potential (RHE), *j* is the current density, *b* is the Tafel slope and *A* is the intercept of the linear regression. The *j*<sub>0</sub> is the current calculated from the Tafel equation by setting  $\eta$  equal to zero. Stability tests are carried out by chronoamperometry measurements (*j-t* curves), *i.e.*, by measuring the current in potentiostatic mode at -0.5 V vs. RHE in 0.5 M H<sub>2</sub>SO<sub>4</sub> over time (200 min).

#### **S.2 X-ray diffraction analysis of bulk MoS<sub>2</sub>, 2H-MoS<sub>2</sub> flakes and 2H-MoS<sub>2</sub> QDs**

X-ray diffraction (XRD) measurements, as reported in Figure 2b of the main text, are used to evaluate the crystal structure of 2H-MoS<sub>2</sub> flakes and QDs with respect to the bulk MoS<sub>2</sub>. Bulk MoS<sub>2</sub> exhibits the characteristic XRD peaks of hexagonal-structure polycrystalline films (JCPDS card no.77-1716).<sup>10</sup> The dominant (002) peak, centered at 14.4°, corresponds to the interlayer d-spacing of 0.614 nm.<sup>11,12</sup> In addition, various weak diffraction reflections are also observed at higher angles, *e.g.*, the ones attributed to the (100), (103), (006), (105), and (008)

planes,<sup>10,12</sup> which are characteristic of polycrystalline MoS<sub>2</sub>.<sup>12</sup> For the 2H-MoS<sub>2</sub> flakes, the intensity of the (002) peak increases with respect to that of bulk MoS<sub>2</sub>, indicating a preferential exposure of (002) basal planes,<sup>11</sup> while all the other diffraction reflections almost disappear, in agreement with the single crystal structure of the few-layered 2H-MoS<sub>2</sub> flakes.<sup>10</sup> In the case of QDs, the intensity of (002) peak is strongly reduced with respect to the bulk material and the 2H-MoS<sub>2</sub> flakes. Similar to 2H-MoS<sub>2</sub> flakes, all the other diffraction peaks disappear.<sup>10</sup> These results indicate that the QDs have the same crystal structure of their native flakes.

### S. 3 Optical absorption spectroscopy of 2H-MoS<sub>2</sub> flakes and 2H-MoS<sub>2</sub> QDs

Figure 2c in the main text shows the absorption spectra of the as-produced 2H-MoS<sub>2</sub> flakes and QDs. For 2H-MoS<sub>2</sub> flakes, the peaks at 660 and 600 nm are ascribed to the A and B excitonic peaks, respectively, arising from the K-point of the Brillouin zone in 2H-MoS<sub>2</sub> flakes.<sup>13,14</sup> Their energy difference (~0.2 eV) arises from the spin-orbit splitting of the valence band in 2H-MoS<sub>2</sub> flakes.<sup>13,15</sup> The distinct peaks at 450 and 395 nm are assigned to direct excitonic C and D inter-band transitions between the density of state peaks in the valence and conduction bands at the M point of the Brillouin zone.<sup>13,16</sup> In the case of 2H-MoS<sub>2</sub> QDs, there are no characteristic excitonic peaks, and the absorption edge is shifted towards lower wavelength with respect to 2H-MoS<sub>2</sub> flakes. This effect could be ascribed to the quantum confinement effect in QDs,<sup>14</sup> which increases their band gap energy with the decrease of the lateral size.<sup>15,17</sup>

### S.4 Photoluminescence characterization of 2H-MoS<sub>2</sub> QDs

The PL spectra of 2H-MoS<sub>2</sub> QD dispersion in IPA, collected at different excitation wavelengths (from 280 to 500 nm) are reported in Figure S1a. The PL peaks are red-shifted with increasing excitation wavelength. This excitation-dependent PL emission is ascribed to quantum confinement<sup>18</sup> and edge state emission effect.<sup>19,20</sup> The sharp small features observed in the spectra are related to the IPA solvent, as observed in its blank PL spectrum (Figure S1b).

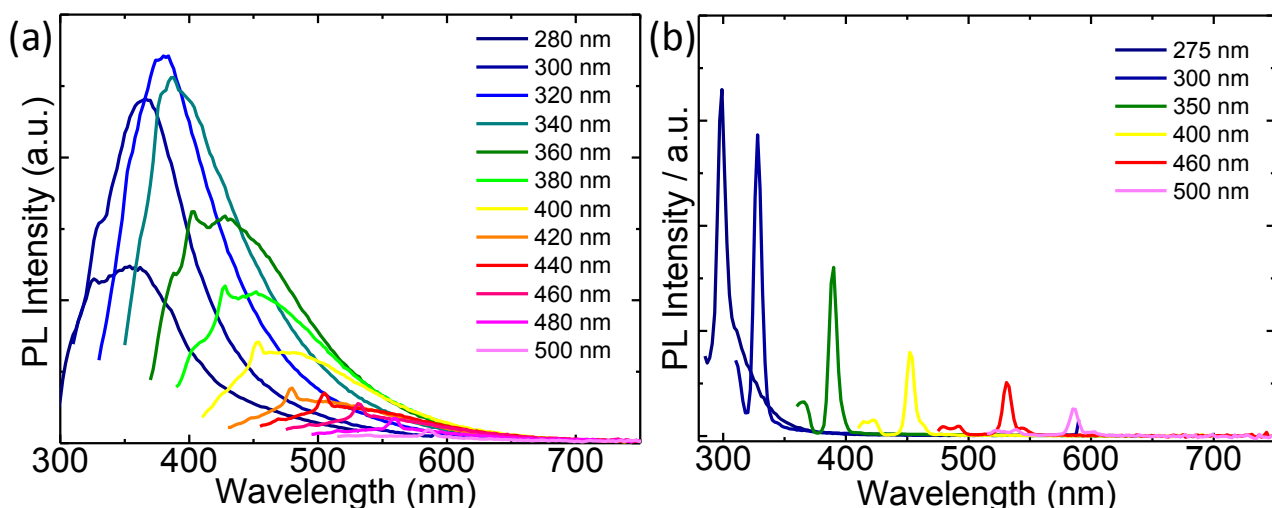


**Figure S1** (a) Photoluminescence spectra of the 2H-MoS<sub>2</sub> QDs at different excitation wavelength (*i.e.*, ranging from 280 to 500 nm). (b) Blank (control) PL measurements of IPA at different excitation wavelengths.

## S.5 Raman analysis of bulk MoS<sub>2</sub>, 2H-MoS<sub>2</sub> flakes, 2H-MoS<sub>2</sub> QDs and 1T-MoS<sub>2</sub> flakes

Raman spectroscopy measurements, reported in Figure 2d of the main text, are carried out to investigate the vibrational modes of 2H-MoS<sub>2</sub> flakes and QDs with respect to those of bulk MoS<sub>2</sub>. The full width at half maximum of the  $E_{2g}^1(\Gamma)$  and  $A_{1g}(\Gamma)$  (FWHM( $E_{2g}^1(\Gamma)$ ) and FWHM( $A_{1g}(\Gamma)$ ), respectively) of both 2H-MoS<sub>2</sub> flakes and QDs increases of  $\sim 3 \text{ cm}^{-1}$  and  $\sim 2 \text{ cm}^{-1}$ , respectively, compared to the corresponding modes of bulk MoS<sub>2</sub>. The increase of FWHM( $A_{1g}(\Gamma)$ ) for 2H-MoS<sub>2</sub> flakes and QDs is attributed to the variation of interlayer force constants between the inner and outer layers.<sup>21</sup>

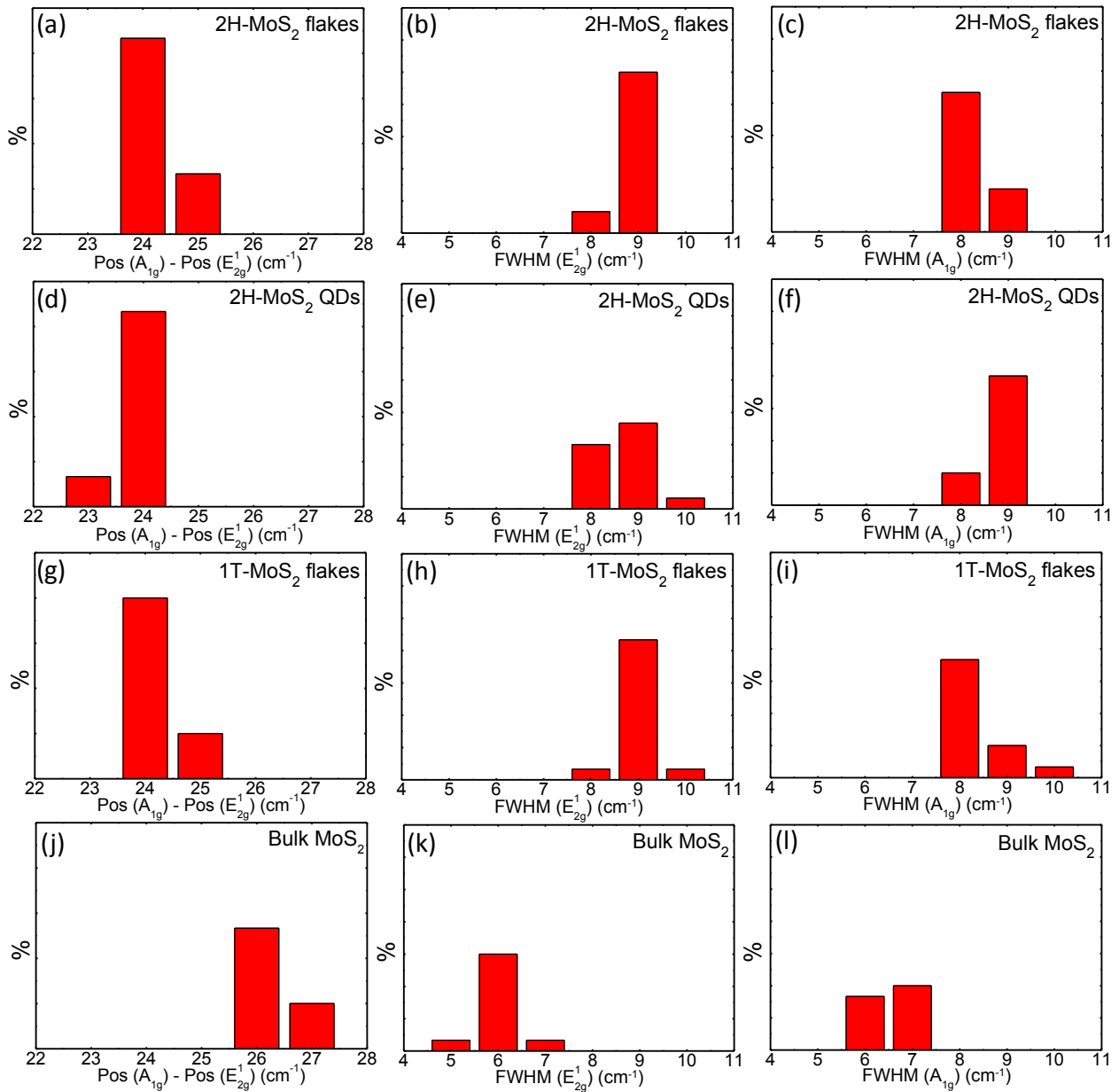


**Figure S2** Statistical Raman analysis of (a) Pos( $A_{1g}$ ) - Pos( $E_{2g}^1$ ), (b) FWHM( $E_{2g}^1$ ) and (c) FWHM( $A_{1g}$ ) for 2H-MoS<sub>2</sub> flakes; (d) Pos( $A_{1g}$ ) - Pos( $E_{2g}^1$ ), (e) FWHM( $E_{2g}^1$ ) and (f) FWHM( $A_{1g}$ ) for 2H-MoS<sub>2</sub> QDs; (g) Pos( $A_{1g}$ ) - Pos( $E_{2g}^1$ ), (h) FWHM( $E_{2g}^1$ ) and (i) FWHM( $A_{1g}$ ) for 1T-MoS<sub>2</sub> flakes; (j) Pos( $A_{1g}$ ) - Pos( $E_{2g}^1$ ), (k) FWHM( $E_{2g}^1$ ) and (l) FWHM( $A_{1g}$ ) for bulk MoS<sub>2</sub>.

Figure S2 shows the statistical Raman analysis of the peak position difference of the  $A_{1g}(\Gamma)$  and  $E_{2g}^1(\Gamma)$  modes, *i.e.*  $\text{Pos}(A_{1g}) - \text{Pos}(E_{2g}^1)$ ,  $\text{FWHM}(E_{2g}^1)$  and  $\text{FWHM}(A_{1g})$  for 2H-MoS<sub>2</sub> flakes (Figure S2a, Figure S2b and Figure S2c, respectively), 2H-MoS<sub>2</sub> QDs (Figure S2d, Figure S2e and Figure S2f, respectively), 1T-MoS<sub>2</sub> flakes (Figure S2g, Figure S2h and Figure S2i, respectively) and bulk MoS<sub>2</sub> (Figure S2j, Figure S2k and Figure S2l, respectively).

Figure S3 shows the Raman spectra of bulk MoS<sub>2</sub>, 2H-MoS<sub>2</sub> flakes, 2H-MoS<sub>2</sub> QDs, and 1T-MoS<sub>2</sub> flakes in the 200-900 cm<sup>-1</sup> range. The data do not reveal additional peaks in the 200-900 cm<sup>-1</sup> range related to molybdenum oxide species,<sup>22</sup> such as the MoO<sub>3</sub> bands located at ~285 cm<sup>-1</sup> ( $B_{2g}$ ,  $B_{3g}$ ), ~666 cm<sup>-1</sup> ( $B_{2g}$ ,  $B_{3g}$ ) and ~820 cm<sup>-1</sup> ( $A_g$ ,  $B_{1g}$ )<sup>23</sup> or the MoO<sub>2</sub> band located at ~203 cm<sup>-1</sup>, ~228 cm<sup>-1</sup>, ~345 cm<sup>-1</sup>, ~363 cm<sup>-1</sup>, ~461 cm<sup>-1</sup>, ~495 cm<sup>-1</sup>, ~571 cm<sup>-1</sup>, ~589 cm<sup>-1</sup> and ~744 cm<sup>-1</sup>.<sup>24</sup> The peaks located at ~520 cm<sup>-1</sup> and ~303 cm<sup>-1</sup> are attributed to the transverse optical (TO) and the second-order transverse acoustic (2TA) phonon modes of Si<sup>25,26,27</sup> (samples are deposited onto Si/SiO<sub>2</sub> substrates), respectively.

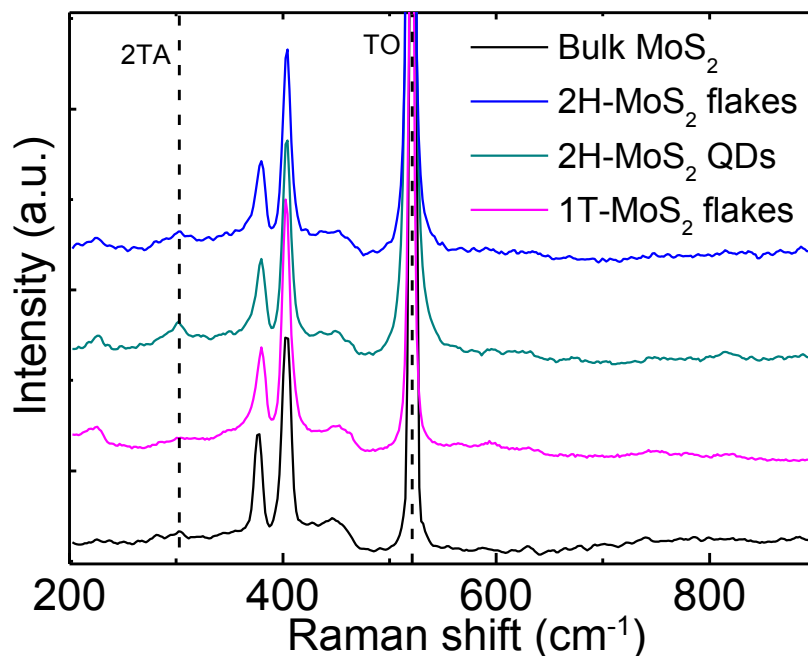


**Figure S3** Extended Raman spectra of the bulk MoS<sub>2</sub> (black), 1T-MoS<sub>2</sub> (magenta), 2H-MoS<sub>2</sub> flakes (blue) and 2H-MoS<sub>2</sub> QDs (cyan). The peaks located at ~520 cm<sup>-1</sup> and 303 cm<sup>-1</sup> are ascribed to the transverse optical (TO) and the second-order transverse acoustic (2TA) phonon modes of Si are indicated by black vertical dashed lines

## S.6 Optical, morphological and chemical characterization of graphene flakes

### S.6.1 Optical absorption spectroscopy analysis of graphene flakes

The OAS measurement of the as-produced graphene flakes dispersion in NMP (1:10 diluted) is reported in Figure S4. The peak at ~265 nm, is a signature of the van Hove singularity in the graphene density of states.<sup>28</sup> The concentration of graphene flakes in dispersion is determined from the optical absorption coefficient at 660 nm, using  $A = \alpha lc$  where  $l$  [m] is the light path length,  $c$  [g L<sup>-1</sup>] is the concentration of dispersed graphitic material, and  $\alpha$  [L g<sup>-1</sup> m<sup>-1</sup>] is the absorption coefficient, with  $\alpha \sim 1390$  L g<sup>-1</sup> m<sup>-1</sup> at 660 nm.<sup>28,29</sup> The obtained concentrations for the 1:10 diluted as-produced graphene flakes dispersion is 0.32 g L<sup>-1</sup>.

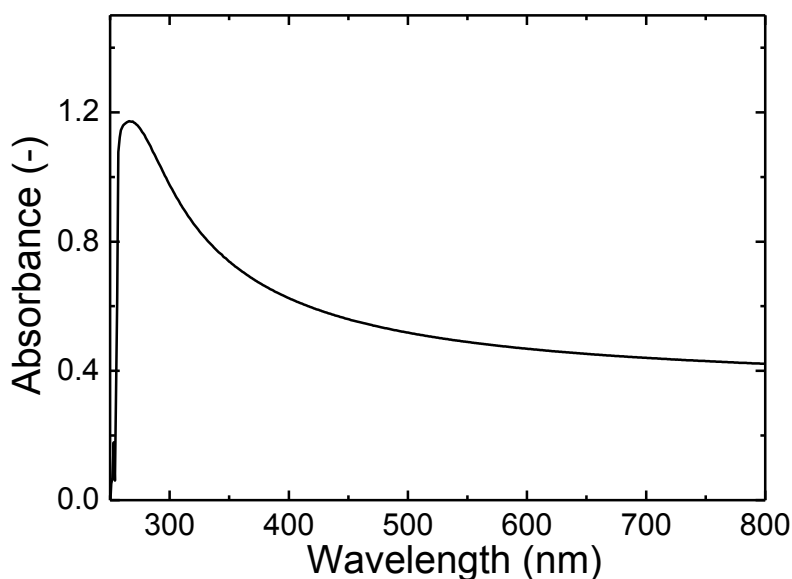


**Figure S4** Absorption spectrum of the 1:10 diluted as-produced graphene flakes dispersion in NMP.

### S.6.2. Raman spectrum and statistical Raman analysis of graphene flakes

The as-produced graphene flakes are characterized by means of Raman spectroscopy. A typical Raman spectrum of defect-free graphene shows, as fingerprints, G and D peaks.<sup>30</sup> The G peak corresponds to the  $E_{2g}$  phonon at the Brillouin zone center.<sup>31</sup> The D peak is due to the breathing modes of  $sp^2$  rings and requires a defect for its activation by double resonance.<sup>30,32,33</sup> The 2D peak is the second order of the D peak,<sup>34</sup> being a single peak in monolayer graphene, whereas it splits in four in bi-layer graphene, reflecting the evolution of the band structure.<sup>30</sup> The 2D peak is always seen, even in the absence of D peak, since no defects are required for the activation of two phonons with the same momentum, one backscattered from the other.<sup>34</sup> Double resonance can also happen as intra-valley process, *i.e.*, connecting two points belonging to the same cone around K or K'.<sup>34</sup> This process gives rise to the D' peak for defective graphene.<sup>34</sup> The D+D' is the combination mode of D and D' while the 2D' is the second order of the D'.<sup>34</sup> As in the case of 2D, 2D' is always seen even when the D' peak is not present.<sup>34</sup> Figure S5a reports a representative Raman spectrum of the as-produced graphene flakes, showing all the bands above described.

The statistical analysis of the position of G (Pos(G)) (Figure S5b), the full width half maximum of G (FWHM(G)) (Figure S5c), the position of 2D (Pos(2D)) (Figure S5d), the full width half maximum of 2D (FWHM(2D)) (Figure S5e), the intensity ratio between the 2D and G peaks ( $I(2D)/I(G)$ ) (Figure S5f) and the intensity ratio between the D and G peaks ( $I(D)/I(G)$ ) (Figure S5i) give useful quantitative information on the graphene flake characteristics. In particular, the Pos(2D) is at  $\sim 2700\text{ cm}^{-1}$  (Figure S5d) while the FWHM(2D) ranges from 60 to 75  $\text{cm}^{-1}$  (Figure S5e). These values are ascribed to few-layer graphene (FLG).<sup>4,30,35</sup> The  $I(2D)/I(G)$  varies from 0.6 to 1.2 (Figure S5f), as expected from a combination of single-layer graphene (SLG) and FLG.<sup>30,36</sup> The presence of D and D' indicate, as discussed for D, the defective nature of the graphene flakes.<sup>34,37,38,39</sup> Previous studies on graphene flakes produced by LPE have shown that these defects are predominantly located at the edges, while the basal plane of the flakes is defect-free.<sup>38,39</sup> This is demonstrated by the absence of correlation between  $I(D)/I(G)$  and FWHM(G).<sup>37,39</sup>



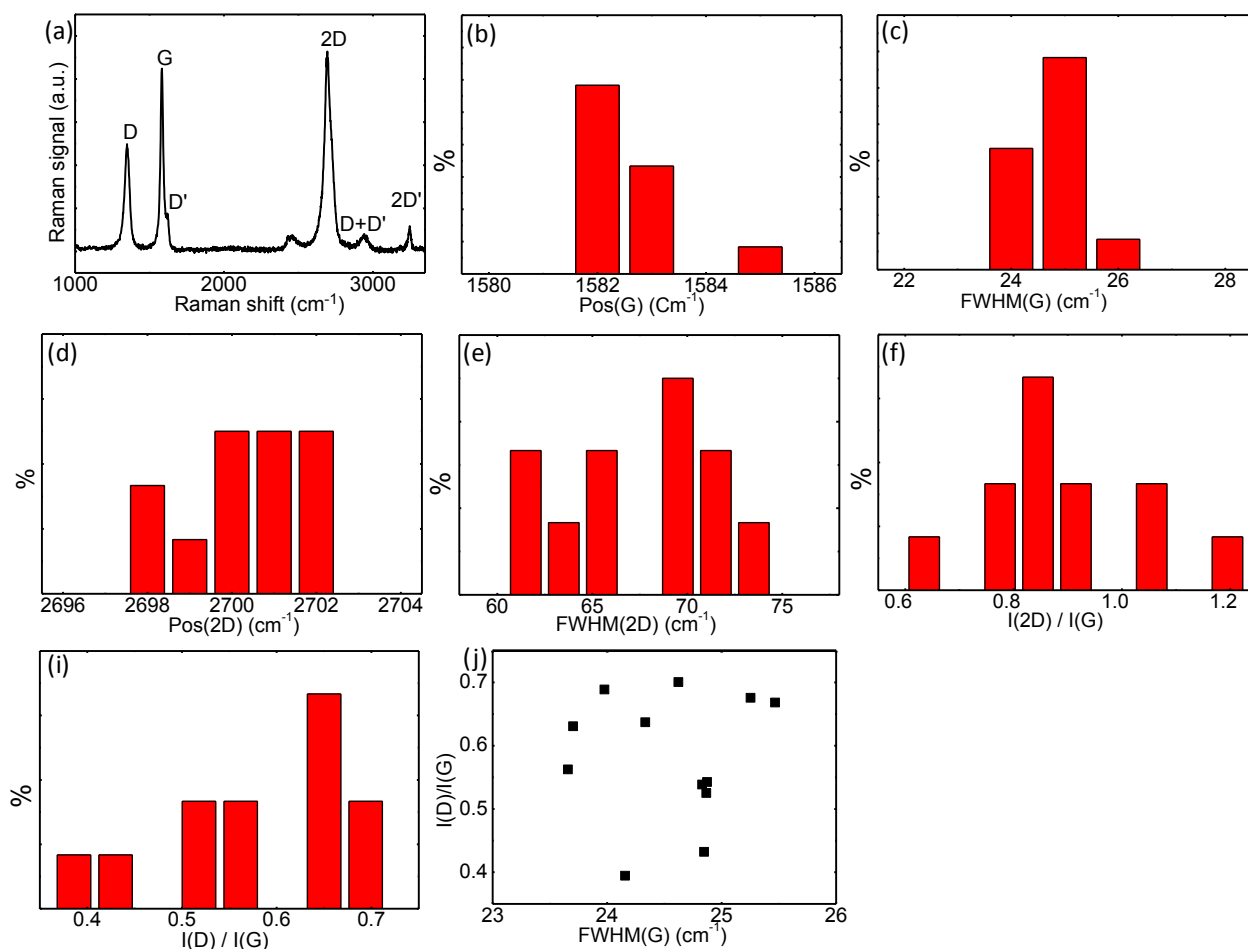


**Figure S5** (a) Representative Raman spectrum of the as produced SLG/FLG by LPE in NMP. The D, G, D', 2D, D+D' and 2D' bands are also denoted. (b) Statistical Raman analysis of the Pos (G), (c) FWHM(G), (d) Pos(2D), (e) FWHM(2D), (f) I(2D)/I(G), (g) I(D)/I(G) and (h) I(D)/I(G) vs. FWHM(G) plot.

Figure S5g shows the statistical analysis of I(D)/I(G), which varies between 0.3 and 0.7, while Figure S5h does not show, in agreement with literature data,<sup>37,39</sup> any correlation between I(D)/I(G) and FWHM(G), thus proving defect-free basal planes of the as produced graphene flakes.

### S.6.3 Morphological characterization of graphene flakes

The morphology of the as-produced graphene flakes is characterized by means of TEM and AFM. Figure S6a shows a representative TEM image of graphene flakes, which have irregular shape and rippled morphology. Statistical TEM analysis of the flakes lateral dimension indicates values distributed in the range of 200-1500 nm and an average value of ~450 nm.

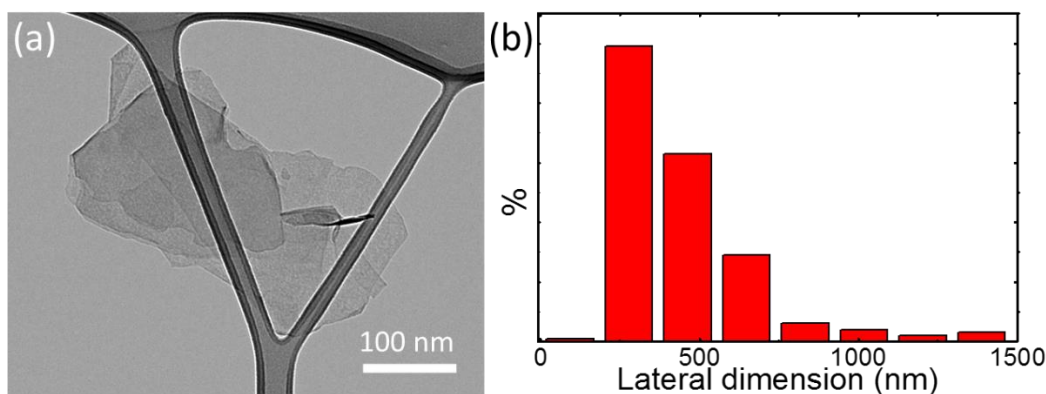


**Figure S6** (a) TEM images of the as-produced graphene flakes and (b) TEM statistical analysis of their lateral dimension.

Figure S7a shows a representative AFM image of graphene flakes. The main thickness distribution is in the 0.5-4 nm range (Figure S7b), with the presence of few thicker flakes (>5 nm). Thus, the sample is mostly composed by a combination of SLG and FLG flakes, in agreement with Raman spectroscopy analysis (see Section S6.2).

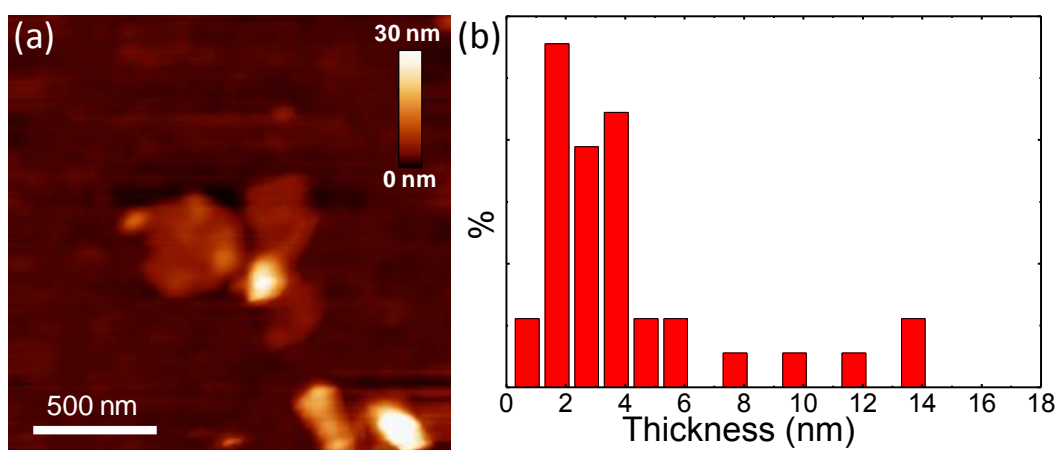


**Figure S7** (a) AFM images of the as-produced graphene flakes and (b) AFM statistical analysis of their lateral dimension.

#### S.6.4 X-ray photoemission spectroscopy analysis of graphene flakes

X-ray photoelectron spectroscopy (XPS) measurements are carried out on as-produced graphene flakes to ascertain their chemical composition. The results are shown in Figure S8. The C 1s spectrum of the graphene flakes (Figure S8a), shows the presence of oxidized C-O and C=O groups at binding energies 286.4 eV and 288.3 eV respectively.<sup>40</sup> The percentage content (%c) of C=O and C-O is ~8%. However, these groups are also attributed to the presence of residual solvent molecule of NMP. In fact, N 1s spectrum (Figure S8b) indicates a %c of NMP ~3.5%. Take into account the NMP contribution in the %c of the oxidized groups, these results confirm that high-quality graphene flakes (%c >95%) are effectively obtained by LPE in NMP, in agreement with previous studies.<sup>41</sup>

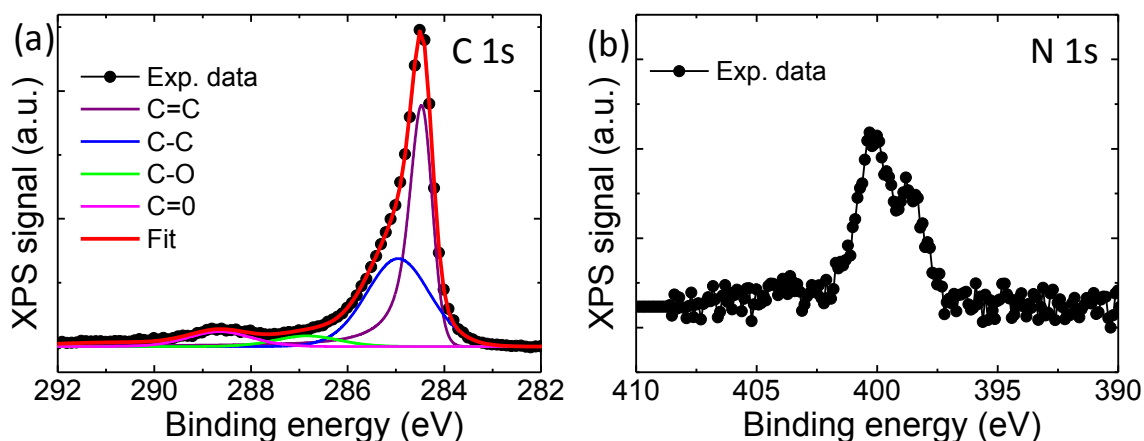


**Figure S8** (a) C 1s and b) N 1s XPS spectra of the graphene flakes sample produced by LPE of graphite in NMP. The deconvolution of C 1s XPS spectra is also shown, indicating the contribution of C=C (purple), C-C (blue), C-O (green), C=O (magenta).

### S.7 Morphology characterization of the hybrid graphene flakes/2H-MoS<sub>2</sub> flakes and graphene flakes/2H-MoS<sub>2</sub> QDs heterostructures

The morphology of the different flexible heterostructures, fabricated by the sequential deposition of graphene and MoS<sub>2</sub> dispersions on nylon membranes, is analysed by using AFM. Figure S9 shows the representative  $1.5 \times 1.5 \mu\text{m}^2$  AFM topographies of the graphene, graphene/2H-MoS<sub>2</sub> flakes, and graphene/2H-MoS<sub>2</sub> QDs flexible electrodes (Figure S9a,d,g), as well as, their respective AFM phase images (Figure S9b,e,h) and AFM 3D images (Figure S9c,f,i). The analysis of the roughness derived from Figure S9 a, d and g reveals the lowest roughness ( $R_a = 10 \text{ nm}$ ;  $RMS = 15 \text{ nm}$ ) in the case of graphene/2H-MoS<sub>2</sub> QDs where the presence of graphene flakes is not observed. In the other two cases, the uniform coverage of the surface with layered material reported roughness of  $R_a = 16 \text{ nm}$ ;  $RMS = 20 \text{ nm}$  and  $R_a = 25 \text{ nm}$ ;  $RMS = 31 \text{ nm}$  for graphene and graphene/2H-MoS<sub>2</sub> flakes electrodes, respectively. The homogeneous coverages of the layered material, for graphene and graphene/2H-MoS<sub>2</sub> flakes, and QDs or QDs aggregates in the case of graphene/2H-MoS<sub>2</sub> QDs heterostructures is also confirmed by the AFM phase images displayed in Figure S9b, Figure S9e and Figure S9h, respectively. In fact, these images show the domains of the different overlay materials of the electrodes over the entire imaged areas ( $1.5 \times 1.5 \mu\text{m}^2$ ).

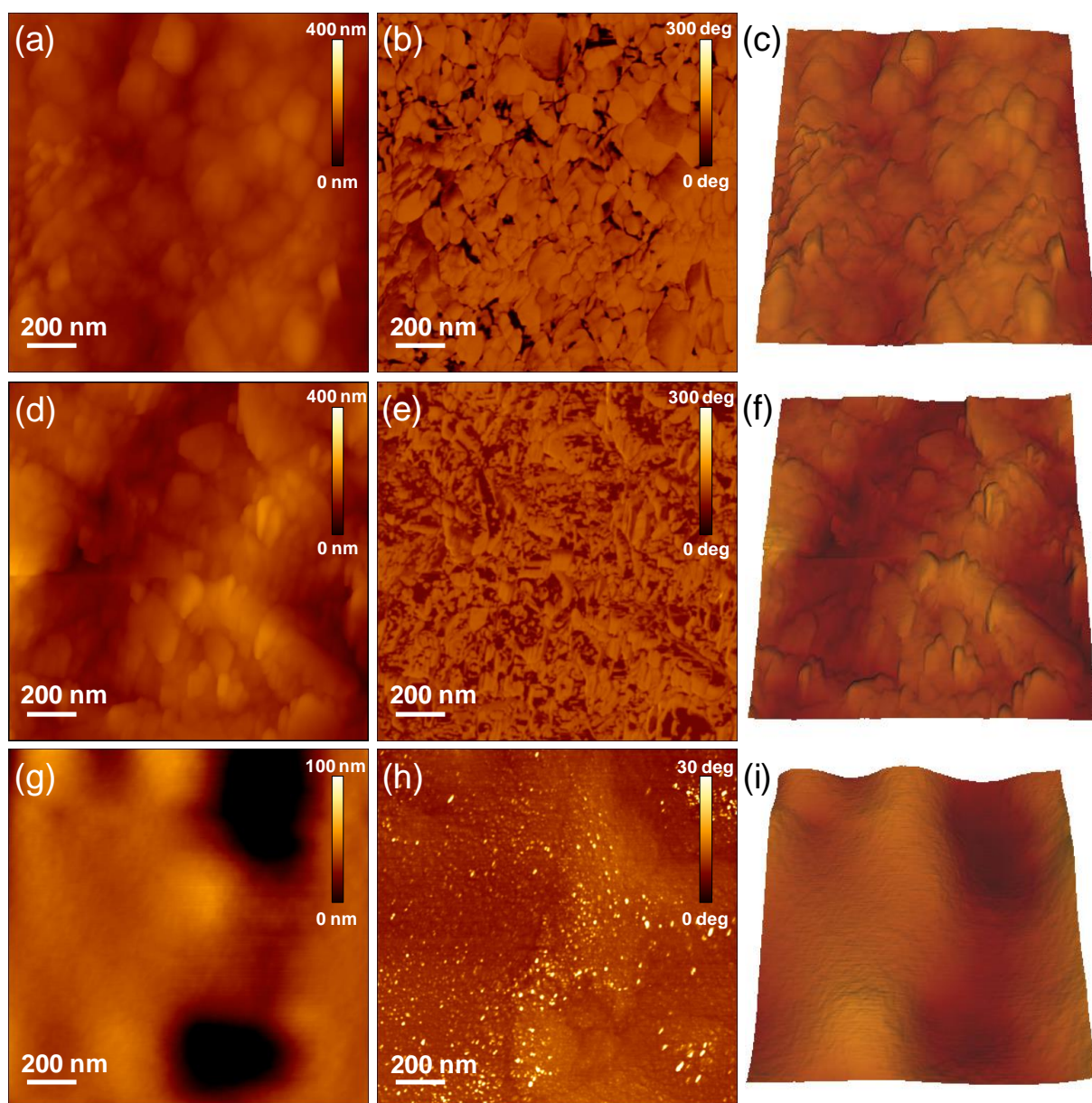


**Figure S9** Atomic force microscopy characterization of the (a-c) graphene, (d-f) graphene/2H-MoS<sub>2</sub> flakes, and (g-i) graphene/2H-MoS<sub>2</sub> QDs flexible electrodes. The AFM topography images of (a) graphene, (d) graphene/2H-MoS<sub>2</sub> flakes, and (g) graphene/2H-MoS<sub>2</sub> QDs flexible electrodes show layered material in the first two cases, while in the case of graphene/2H-MoS<sub>2</sub> QDs it is observed a smoother surface covered by the presence of QDs. The AFM phase images of graphene, graphene/2H-MoS<sub>2</sub> flakes and graphene/2H-MoS<sub>2</sub> QDs flexible electrodes are presented in (b), (e) and (h) respectively, while the corresponding 3D images are shown in (c), (f) and (i), respectively.

## S.8 X-ray photoemission spectroscopy analysis of 1T-MoS<sub>2</sub> flakes and MoS<sub>2</sub> QDs produced from 1T-MoS<sub>2</sub> flakes

The 1T-MoS<sub>2</sub> flakes are obtained by chemical lithium intercalation method.<sup>1</sup> This method results in loss of pristine semiconducting properties of 2H-MoS<sub>2</sub> flakes due to structural changes that occur during Li intercalation, *i.e.*, 1T-MoS<sub>2</sub> flakes formation.<sup>42,43,44,45,46</sup> The morphological and optical characterization of the as-produced 1T-MoS<sub>2</sub> flakes has been recently reported by our group.<sup>47</sup> As main results, the TEM analysis of the 1T-MoS<sub>2</sub> flakes

indicated lateral size in the 30-800 nm range (average value  $\sim 275$  nm), while AFM analysis revealed average thickness of  $2.3 \pm 1.6$  nm. Moreover, XPS analysis revealed that the resulting MoS<sub>2</sub> flakes are a mixture of both 2H and 1T phase. However, the metastable metallic 1T phase dominates the electrocatalytic properties of the as-exfoliated material,<sup>42-46</sup> but mild annealing ( $\sim 100$  °C) leads to gradual restoration of the semiconducting phase.<sup>42</sup> Figure S10a reports the XPS spectra of the as produced 1T-MoS<sub>2</sub> flakes. The peaks located at  $\sim 229$  eV and at  $\sim 232$  eV are assigned to Mo 3d of MoS<sub>2</sub> and fitted by two components, which are attributed to the 2H (green line) and 1T phase (cyan line) of MoS<sub>2</sub> flakes, respectively. Figure S10b shows the XPS spectra of MoS<sub>2</sub> QDs produced starting from the 1T-MoS<sub>2</sub> flakes. Clearly, the 1T phase contribution is reduced with respect to the one observed in 1T-MoS<sub>2</sub> flakes, indicating that the solvothermal treatment causes a 1T-to-2H phase conversion. These results prove that it is challenging to produce 1T-MoS<sub>2</sub> QDs from 1T-MoS<sub>2</sub> flakes because of the intrinsic metastable nature of the latter.<sup>48,49,50</sup>

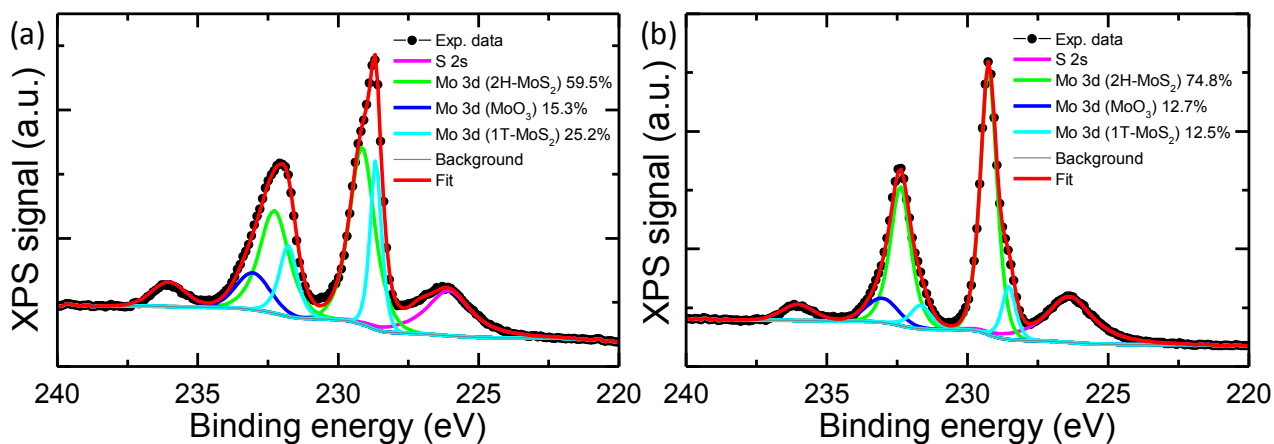


**Figure S10** Mo 3d and S 2s XPS spectra for (a) 1T-MoS<sub>2</sub> flakes and (b) the MoS<sub>2</sub> QDs derived from 1T-MoS<sub>2</sub> flakes. Their deconvolutions are shown, indicating the contribution of both 1T and 2H phase of MoS<sub>2</sub> for Mo 3d peaks (solid cyan and green lines, respectively). The S 2s band of MoS<sub>2</sub> and Mo 3d bands of MoO<sub>3</sub> are also evidenced (solid magenta and blue lines, respectively). The percentage contents of Mo 3d bands attributed to 2H-MoS<sub>2</sub>, 1T-MoS<sub>2</sub> and MoO<sub>3</sub> are also reported in the figure legends.

## S.9 Stability tests of graphene/2H-MoS<sub>2</sub> flakes and graphene/2H-MoS<sub>2</sub> QDs in HER-conditions

The stability of the graphene/2H-MoS<sub>2</sub> flakes and graphene/2H-MoS<sub>2</sub> QDs in hydrogen evolution reaction (HER)-condition is evaluated by chronoamperometry measurements (*j-t* curves) at -0.5 V vs. RHE. Figure S11 shows the results of the tests over 200 min of continuous operation. The graphene/2H-MoS<sub>2</sub> QDs show a progressive HER activation, with an increase of the current of  $\sim 10\%$  after 200 min, while the current of graphene/2H-MoS<sub>2</sub> flakes decrease by  $\sim 4\%$  with respect to the starting values. These results suggest that the catalytic edge sites of 2H-MoS<sub>2</sub> QDs are more resistant toward oxidative/degradation processes, which passivate the HER catalytic sites, with respect to those of 2H-MoS<sub>2</sub> flakes. In fact, density functional theory calculation have shown that oxidation energies for MoS<sub>2</sub> flakes depend on the local competition of binding energy of the covalent bonds at the edge sites,<sup>51</sup> whose nature can be different for 2D and 0D nanostructures.<sup>52</sup>



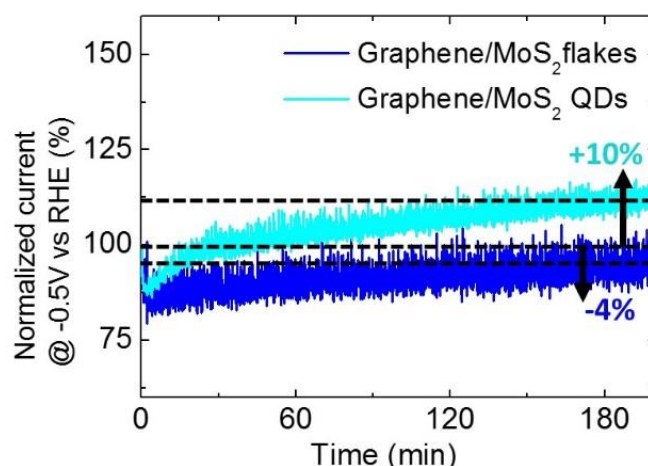


**Figure S11** Chronoamperometry measurements (*j*-*t* curves) at -0.5 V vs. RHE of the graphene/2H-MoS<sub>2</sub> flakes (blue lines) and graphene/2H-MoS<sub>2</sub> QDs (cyan line), over 200 min.

### S.10 Comparison of the HER electrocatalytic activity of the as-produced devices in the literature context

As pointed out in the conclusion of the main text, the HER electrocatalytic performance of our systems (*e.g.* GC/2H-MoS<sub>2</sub> QDs and the graphene/2H-MoS<sub>2</sub> QDs approach that of several MoS<sub>2</sub>-based catalyst reported in literature, overcoming those of recent MoS<sub>2</sub> flakes or MoS<sub>2</sub> QDs synthesized by scalable routes compatible with high-throughput industrial processes.<sup>14,18,53,54,55</sup> The comparison of the HER electrocatalytic activity of our system with other relevant reported findings (not strictly referring to material synthesis compatible with high-throughput industrial processes) is reported in Table S1.

**Table S1** Comparison of HER electrocatalytic activity of our systems with other relevant reported findings

HER electrocatalyst	$\eta_{10}$ (V)	Tafel slope (mV/dec)	reference
Graphene (GC)/2H-MoS <sub>2</sub> QDs	0.136 (0.312)	141 (78)	this work
MoS <sub>2</sub> nanosheets	~0.43	115	53
MoS <sub>2</sub> dots on Au	0.16	82	12
MoS <sub>2</sub> dots/nanosheet hybrid on Au	0.19	74	18
MoS <sub>2</sub> nanodots	~0.28	61	14
Thermal texturized MoS <sub>2</sub>	0.17	~60-70	54
Microdomain reaction-produced MoS <sub>2</sub> nanosheets	~0.19	68	55
H <sub>2</sub> -annealed MoS <sub>2</sub> monolayer	<0.55	147	56
1T-MoS <sub>2</sub> nanosheets	~0.20	40	42
Double-gyroid MoS <sub>2</sub> films	<0.20	50	57
Edge-exposed MoS <sub>2</sub> nano-assembled structures	~0.18/0.19	100	58
stepped edge surface terminated MoS <sub>2</sub> sheet arrays	0.10	59	59
flat edge surface terminated MoS <sub>2</sub> sheet arrays	0.14	69	59
MoS <sub>2</sub> /RGO hybrid	~0.15	41	60

### Acknowledgments

We thank the Electron Microscopy facility - Istituto Italiano di Tecnologia, for support in TEM data acquisition.

## References

- 1 Nicolosi V.; Chhowalla M.; Kanatzidis M. G.; Strano M. S.; Coleman J. N. Liquid exfoliation of layered materials. *Science*, **2013**, *340*, 1226419.
- 2 Bonaccorso, F.; Lombardo, A.; Hasan, T.; Sun, Z.; Colombo, L.; Ferrari, A. C. Production and processing of graphene and 2d crystals. *Mater. Today*, **2012**, *15*, 564-589.
- 3 Bonaccorso, F.; Bartolotta, A.; Coleman, J. N.; Backes, C. 2D-Crystal-Based Functional Inks. *Adv. Mater.*, **2016**, *28*, 6136.
- 4 Maragó, O. M.; Bonaccorso, F.; Saija, R.; Privitera, G.; Gucciardi, P. G.; Iati, M. A.; Calogero, G.; Jones, P. H.; Borghese, F.; Denti, P.; Nicolosi, V. Brownian motion of graphene. *ACS Nano*, **2010**, *4*, 7515-7523.
- 5 Casaluci, S.; Gemmi, M.; Pellegrini, V.; Di Carlo, A.; Bonaccorso, F. Graphene-based large area dye-sensitized solar cell modules. *Nanoscale*, **2016**, *8*, 5368.
- 6 Yuwen L.; Yu H.; Yang X.; Zhou J.; Zhang Q.; Zhang Y.; Wang L. Rapid preparation of single-layer transition metal dichalcogenide nanosheets via ultrasonication enhanced lithium intercalation. *Chem. Comm.*, **2016**, *52*, 529-532.
- 7 Jung Y.; Zhoub Y.; Cha J. J. Intercalation in two-dimensional transition metal chalcogenides. *Inorg. Chem. Front.*, **2016**, *3*, 452-463.
- 8 Vilekar S. A.; Fishtik I.; Datta R. Kinetics of the hydrogen electrode reaction. *J. Electrochem. Soc.*, **2010**, *157*, B1040-B1050.
- 9 Conway B. E.; Tilak B. V. Interfacial processes involving electrocatalytic evolution and oxidation of H<sub>2</sub>, and the role of chemisorbed H. *Electrochim. Acta*, **2002**, *47*, 3571-3594.
- 10 Joensen P.; Crozier E. D.; Alberding N.; Frindt R. F. A study of single-layer and restacked MoS<sub>2</sub> by X-ray diffraction and X-ray absorption spectroscopy, *J. Phys. C: Solid State Phys.*, **1987**, *20*, 4043-4053
- 11 Yue N.; Weicheng J.; Rongguo W.; Guomin D.; Yifan H. Hybrid nanostructures combining graphene–MoS<sub>2</sub> quantum dots for gas sensing. *J. Mater. Chem. A*, **2016**, *4*, 8198-8203
- 12 Wang T.; Gao D.; Zhu J.; Papakonstantinou P.; Li Y.; Li M. X. Size-Dependent Enhancement of Electrocatalytic Oxygen-Reduction and Hydrogen-Evolution Performance of MoS<sub>2</sub> Particles. *Chem.-Eur. J.*, **2013**, *19*, 11939-11948
- 13 Mak K. F.; Lee C.; Hone J.; Shan J.; Heinz T. F. Atomically thin MoS<sub>2</sub>: a new direct-gap semiconductor. *Phys. Rev. Lett.*, **2010**, *105*, 136805.
- 14 Benson, J.; Li, M.; Wang, S.; Wang, P.; Papakonstantinou, P. Electrocatalytic hydrogen evolution reaction on edges of a few layer molybdenum disulfide nanodots, *ACS Appl. Mater. Interfaces*, **2015**, *7*, 14113-14122.
- 15 Wilcoxon J. P.; Samara G. A. Strong quantum-size effects in a layered semiconductor: MoS<sub>2</sub> nanoclusters. *Phys. Rev. B: Condens. Matter Mater. Phys.*, **1995**, *51*, 7299.
- 16 Wilcoxon J. P.; Newcomer P. P.; Samara G. A.; Synthesis and optical properties of MoS<sub>2</sub> and isomorphous nanoclusters in the quantum confinement regime. *J. Appl. Phys.*, **1997**, *81*, 7934-7944
- 17 Muscuso L.; Cravanzola S.; Cesano F.; Scarano D.; Zecchina A. Optical, Vibrational, and structural properties of MoS<sub>2</sub> nanoparticles obtained by exfoliation and fragmentation via ultrasound cavitation in isopropyl alcohol., *J. Phys. Chem. C*, **2015**, *119*, 3791-3801.
- 18 Gopalakrishnan D.; Damien D.; Shaijumon M. M. MoS<sub>2</sub> quantum dot-interspersed exfoliated MoS<sub>2</sub> nanosheets. *ACS Nano*, **2014**, *8*, 5297-5303.
- 19 Gopalakrishnan D.; Damien D.; Li B.; Gullappalli H.; Pillai V. K.; Ajayan P. M.; Shaijumon M. M. Electrochemical synthesis of luminescent MoS<sub>2</sub> quantum dots. *Chem. Commun.*, **2015**, *51*, 6293-6296
- 20 Gan Z.; Xu H.; Hao Y. Mechanism for excitation-dependent photoluminescence from graphene quantum dots and other graphene oxide derivatives: consensus, debates and challenges. *Nanoscale*, **2016**, *8*, 7794-7807
- 21 Lee C.; Yan H.; Brus L. E.; Heinz T. F.; Hone J.; Ryu S. Anomalous lattice vibrations of single- and few-layer MoS<sub>2</sub>. *ACS Nano*, **2010**, *4*, 2695-2700.
- 22 Dieterle M.; Mestl G. Raman spectroscopy of molybdenum oxides Part II. Resonance Raman spectroscopic characterization of the molybdenum oxides Mo<sub>4</sub>O<sub>11</sub> and MoO<sub>2</sub>. *Phys. Chem. Chem. Phys.*, **2002**, *4*, 822-826.
- 23 Py M. A.; Maschke K. Intra- and interlayer contributions to the lattice vibrations in MoO<sub>3</sub>. *Phys. B*, **1981**, *105*, 370-374.

- 24 Spevack P. A.; McIntyre N.S. Thermal reduction of molybdenum trioxide. *J. Phys. Chem.*, **1992**, *96*, 9029-9035.
- 25 Zhang S. L.; Wang X.; Ho K.; Li J.; Diao P.; Cai S. Raman spectra in a broad frequency region of p-type porous silicon. *J. Appl. Phys.*, **1994**, *76*, 3016-3019
- 26 Richter H.; Wang Z. P.; Ley L. The one phonon Raman spectrum in microcrystalline silicon. *Solid State Commun.*, **1981**, *39*, 625-629
- 27 Temple P. A.; Hathaway C. E. Multiphonon Raman spectrum of silicon. *Phys. Rev. B*, **1973**, *7*, 3685.
- 28 Kravets V. G.; Grigorenko A. N.; Nair R. R.; Blake P.; Anissimova S.; Novoselov K. S.; Geim A. K. Spectroscopic ellipsometry of graphene and an exciton-shifted van Hove peak in absorption. *Phys. Rev. B*, **2010**, *81* 155413.
- 29 Lotya M.; Hernandez Y.; King P. J.; Smith R. J.; Nicolosi V.; Karlsson L. S.; Blighe F. M.; De S.; Zhiming W.; McGovern I. T.; Duesberg G. S.; Coleman J. N. Liquid phase production of graphene by exfoliation of graphite in surfactant/water solutions. *J. Am. Chem. Soc.*, **2009**, *131*, 3611-3620.
- 30 Ferrari A. C.; Meyer J. C.; Scardaci V.; Casiraghi C.; Lazzeri M.; Mauri F.; Piscanec S.; Jiang D.; Novoselov K. S.; Roth S.; Geim A. K. Raman spectrum of graphene and graphene layers. *Phys. Rev. Lett.*, **2006**, *97*, 187401.
- 31 Ferrari A. C.; Basko D. M. Raman spectroscopy as a versatile tool for studying the properties of graphene. *Nat. Nanotechnol.*, **2013**, *8*, 235-246
- 32 Ferrari A. C.; Robertson J. Interpretation of Raman spectra of disordered and amorphous carbon. *Phys. Rev. B*, **2000**, *61*, 14095-14107
- 33 Ferrari A. C.; Robertson J. Resonant Raman spectroscopy of disordered, amorphous, and diamondlike carbon. *Phys. Rev. B*, **2001**, *64*, 075414.
- 34 Su C.-Y.; Xu Y.; Zhang W.; Zhao J.; Tang X.; Tsai C.-H.; Li L.-J. Electrical and spectroscopic characterizations of ultra-large reduced graphene oxide monolayers. *Chem. Mater.*, **2009**, *21*, 5674.
- 35 Hassoun J.; Bonaccorso F.; Agostini M.; Angelucci M.; Betti M. G.; Cingolani R.; Gemmi M.; Mariani C.; Panero S.; Pellegrini V.; Scrosati B. An advanced lithium-ion battery based on a graphene anode and a lithium iron phosphate cathode. *Nano Lett.*, **2014**, *14*, 4901-4906
- 36 Graf D.; Molitor F.; Ensslin K.; Stampfer C.; Jungen A.; Hierold C.; Wirtz L. Spatially resolved Raman spectroscopy of single- and few-layer graphene. *Nano Lett.*, **2007**, *7*, 238-242
- 37 Bracamonte M. V.; Lacconi G. I.; Urreta S. E.; Foa Torres L. E. F. On the nature of defects in liquid-phase exfoliated graphene. *J. Phys. Chem. C*, **2014**, *118*, 15455-15495.
- 38 Lotya M.; Hernandez Y.; King P. J.; Smith R. J.; Nicolosi V.; Karlsson L. S.; Blighe F. M.; De S.; Wang Z. M.; McGovern I. T.; Duesberg G. S.; Coleman J. N. *J. Am. Chem. Soc.*, **2009**, *131*, 3611-3620.
- 39 Coleman J. N. Liquid phase production of graphene by exfoliation of graphite in surfactant/water solutions. *Acc. Chem. Res.*, **2013**, *46*, 14.
- 40 Yang D.; Velamakanni A.; Bozoklu G.; Park S.; Stoller M.; Piner R. D.; Stankovich S.; Jung I.; Field D.; Ventrone C. A.; Ruoff R. S. Chemical analysis of graphene oxide films after heat and chemical treatments by X-ray photoelectron and Micro-Raman spectroscopy. *Carbon*, **2009**, *47*, 145.
- 41 Buzio, R.; Gerbi, A.; Bernini, C.; Del Rio Castillo, A. E.; Palazon, F.; Siri, A. S.; Pellegrini, V.; Pellegrino, L.; Bonaccorso, F. Ultralow friction of ink-jet printed graphene flakes. *Nanoscale*, **2017**, *in press*.
- 42 Voiry D.; Salehi M.; Silva R.; Fujita T.; Chen M.; Asefa T.; Shenoy V. B.; Eda G.; Chhowalla M. Conducting MoS<sub>2</sub> nanosheets as catalysts for hydrogen evolution reaction. *Nano Lett.*, **2013**, *13*, 6222-6227.
- 43 Ambrosi A.; Sofer Z.; Pumera M. Lithium intercalation compound dramatically influences the electrochemical properties of exfoliated MoS<sub>2</sub>. *Small*, **2015**, *11*, 5, 605-612.
- 44 Py M. A.; Haering R. R. Structural destabilization induced by lithium intercalation in MoS<sub>2</sub> and related compounds. *Can. J. Phys.*, **1983**, *61*, 76-84
- 45 Kertesz M.; Hoffmann R. Octahedral vs. trigonal-prismatic coordination and clustering in transition-metal dichalcogenides. *J. Am. Chem. Soc.*, **1984**, *106*, 3453-3460.
- 46 Chhowalla M.; Shin H. S.; Eda G.; Li L.-J.; Loh K. P.; Zhang H. The chemistry of two-dimensional layered transition metal dichalcogenide nanosheets. *Nature Chem.*, **2013**, *5*, 263.
- 47 Bellani S.; Najafi L.; Capasso A.; Del Rio Castillo A. E.; Antognazza M. R.; Bonaccorso F. Few-layer MoS<sub>2</sub> flakes as a hole-selective layer for solution-processed hybrid organic hydrogen-evolving photocathodes. *J. Mater. Chem. A*, **2017**, *5*, 4384-4396.



- 48 Gao G.; Jiao Y.; Ma F.; Jiao Y.; Wacławik E.; Du A. Charge mediated semiconducting-to-metallic phase transition in molybdenum disulfide monolayer and hydrogen evolution reaction in new 1T' phase. *J. Phys. Chem. C*, **2015**, *119*, 13124-13128.
- 49 Voiry D.; Yamaguchi H.; Li J.; Silva R.; Alves D. C. B.; Fujita T.; Chen M.; Asefa T.; Shenoy V. B.; Eda G.; Chhowalla M. Enhanced catalytic activity in strained chemically exfoliated WS<sub>2</sub> nanosheets for hydrogen evolution. *Nature Mater.*, **2013**, *12*, 850-855.
- 50 Tsai H. L.; Heising J.; Schindler J. L.; Kannewurf C. R.; Kanatzidis M. G. Exfoliated-restacked phase of WS<sub>2</sub>. *Chem. Mater.*, **1997**, *9*, 879-882.
- 51 Liang T.; Sawyer W. G.; Perry S. S.; Sinnott S. B.; Phillpot S. R. Energetics of Oxidation in MoS<sub>2</sub> Nanoparticles by Density Functional Theory. *J. Phys. Chem. C*, **2011**, *115*, 10606-10616.
- 52 Mukherjee S.; Maiti R.; Katiyar A. K.; Das S.; Ray S. K. Novel Colloidal MoS<sub>2</sub> Quantum Dot Heterojunctions on Silicon Platforms for Multifunctional Optoelectronic Devices. *Sci. Rep.*, **2016**, *6*, 29016.
- 53 Varrla E.; Backes C.; Paton K. R.; Harvey A.; Gholamvand Z.; McCauley J.; Coleman J. N.; Large-scale production of size-controlled MoS<sub>2</sub> nanosheets by shear exfoliation. *Chem. Mater.*, **2015**, *27*, 1129-1139.
- 54 Kiriya D.; Lobaccaro P.; Nyein H. Y. Y.; Taheri P.; Hettick M.; Shiraki H.; Sutter-Fella C. M.; Zhao P.; Gao W.; Maboudian R.; Ager J. W.; Javey A. General Thermal Texturization Process of MoS<sub>2</sub> for Efficient Electrocatalytic Hydrogen Evolution Reaction. *Nano Lett.*, **2016**, *16*, 4047-4053.
- 55 Wu Z.; Fang B.; Wang Z.; Wang C.; Liu Z.; Liu F.; Wang W.; Alfantazi A.; Wang D.; Wilkinson D. P. MoS<sub>2</sub> nanosheets: a designed structure with high active site density for the hydrogen evolution reaction. *ACS Catal.*, **2013**, *3*, 2101-2107.
- 56 Ye G.; Gong Y.; Lin J.; Li B.; He Y.; Pantelides S. T.; Zhou W.; Vajtai R.; Ajayan P. M. Defects engineered monolayer MoS<sub>2</sub> for improved hydrogen evolution reaction. *Nano Lett.*, **2016**, *16*, 1097-1103.
- 57 Kibsgaard J.; Chen Z.; Reinecke B. N.; Jaramillo T. F. Engineering the surface structure of MoS<sub>2</sub> to preferentially expose active edge sites for electrocatalysis. *Nat. Mater.*, **2012**, *11*, 963-969.
- 58 Chung D. Y.; Park S. K.; Chung Y. H.; Yu S. H.; Lim D. H.; Jung N.; Ham H. C.; Park H. Y.; Piao Y.; Yoo S. J.; Sung Y. E. Edge-exposed MoS<sub>2</sub> nano-assembled structures as efficient electrocatalysts for hydrogen evolution reaction. *Nanoscale*, **2014**, *6*, 2131-2136.
- 59 Hu J.; Huang B.; Zhang C.; Wang Z.; An Y.; Zhou D.; Lin H.; Leung M. K.; Yang S. Engineering stepped edge surface structures of MoS<sub>2</sub> sheet stacks to accelerate the hydrogen evolution reaction. *Energy Environ. Sci.*, **2017**, *10*, 593.
- 60 Li Y.; Wang H.; Xie L.; Liang Y.; Hong G.; Dai H. MoS<sub>2</sub> nanoparticles grown on graphene: an advanced catalyst for the hydrogen evolution reaction. *J. Am. Chem. Soc.*, **2011**, *133*, 7296-7299.